Mech. Sci., 17, 769–782, 2026
https://doi.org/10.5194/ms-17-769-2026

Mechanical Sciences
Open Access

Mechanical responses of high-speed train derailment due to collision with deformable obstacles

Lingxiang Kong[1], **Shuguang Yao**[2], **and Dongtao Wang**[1,2,3]

[1]School of Vehicle Engineering, Hunan Automotive Engineering Vocational University, Zhuzhou, 412001, China
[2]The State Key Laboratory of Heavy-duty and Express High-power Electric Locomotive, Central South University, Changsha, 410075, China
[3]CRRC Zhuzhou Institute Co., Ltd., Zhuzhou 412001, China

Correspondence: Dongtao Wang (dongtao_wang@csu.edu.cn)

Received: 22 April 2026 – Revised: 17 May 2026 – Accepted: 3 June 2026 – Published: 27 July 2026

Abstract. The collision phenomenon of high-speed trains colliding with obstacles is prone to resulting in derailment. This study focuses on analyzing the mechanical responses of a high-speed train when colliding with a deformable obstacle at different angles and speeds. The results show that the derailment initiation speed decreases with the increase in angle. Overall, as the angle increased from 0 to 45°, derailment risk increased. Specifically, when the speed was $110\,\mathrm{km\,h^{-1}}$ and the angle was 45°, the wheels of the front bogie of the head train derailed; by contrast, no derailment occurred for collision angles ranging from 0 to 40°. When the angle was lower than 5°, derailment did not occur even when the speed increased up to the train's design speed of $250\,\mathrm{km\,h^{-1}}$. Jumping derailment and climbing derailment were observed, respectively, when the collision angle ranged from 10 to 25° and from 30 to 45°. It was revealed that derailment occurred due to the combined effect of lateral and vertical forces acting on the contact interface. By establishing a derailment boundary incorporating both collision angle and speed parameters, the research provides valuable insights for railway infrastructure design and safety speed limit determination in high-speed rail operations.

1 Introduction

The high-speed railway network in China is experiencing rapid development, accompanied by continuous improvements in operational speed, service coverage, and transportation efficiency. Alongside such remarkable progress, however, the occurrence of train collision accidents has gradually increased, posing persistent challenges to the operational safety of rail transit systems. Among various types of railway accidents, those induced by train derailment account for an extremely high proportion, reaching up to 60 % of all collision-related incidents (Liu et al., 2017). As emphasized in official reports issued by the Federal Railroad Administration, unexpected obstacles intruding onto the track are recognized as one of the primary causal factors leading to sudden train derailment during normal operation (Ling et al., 2016a). These obstacles cover a wide spectrum of real-world scenarios, including trucks and other road vehicles stranded or improperly traversing level crossings (Ling et al., 2016b, 2017), urban trams intersecting with main railway lines (Zhou et al., 2013), aged or deformed tunnel infrastructure (Yan et al., 2020), station platforms (Li et al., 2023), bridge abutments (Zhang and Li, 2023), and unattended maintenance equipment temporarily left on the rails during engineering operations (Ling et al., 2019). In sections of railway lines without fully enclosed protective fencing, large domestic animals such as pigs and cows (Lu et al., 2021), as well as wild animals including moose (Peng et al., 2023), may also enter the track zone unexpectedly and become hazardous obstacles that trigger severe collisions.

Compared with collisions involving conventional road vehicles (Neves et al., 2018), train derailment accidents tend to result in significantly more catastrophic consequences, including heavy casualties, extensive structural damage, and prolonged disruptions to transportation systems (Liu et al., 2012; Madsen et al., 2024). A representative and tragic example is the accident involving Taiwan's Taroko Express train, which collided with a construction vehicle that slid onto the rail, leading to severe train derailment and more than 200 casualties (Jiang and Chen, 2021). This disastrous accident strongly highlights the urgent necessity of systematically investigating the derailment mechanism of trains during collisions with track obstacles, so as to support the development of effective prevention and mitigation measures for future rail safety management.

Obstacles involved in train collisions exhibit diverse physical and mechanical properties, leading to highly variable mechanical responses during the impact process. For instance, Ling et al. (2017) suggested that the lateral displacement of the train induced by lateral impact forces represents the fundamental cause of derailment when trains collide with trucks at level crossings. For inclined trucks, Zhuo et al. (2023) further concluded that lateral wheel-set displacement and wheel lift-off from the rail surface are the dominant mechanisms responsible for train derailment. In addition, the collision angle and initial impact speed have been widely identified as critical parameters that significantly govern the dynamic collision response and subsequent operational stability of trains (Zhang and Li, 2023; Yao et al., 2020; Yao et al., 2019; Zhang et al., 2021; Hou et al., 2020). Nevertheless, most existing studies focus on fixed collision conditions; few have established derailment boundaries or classify derailment modes for deformable obstacles.

In practical engineering situations, trains may collide with obstacles across a wide range of speeds and intrusion angles, under which the dynamic responses and stability boundaries may change substantially and potentially lead to derailment. For deformable obstacles in particular, significant large-scale deformation and energy absorption occur during the collision process (Cho and Koo, 2012; Yuan et al., 2026), causing continuous variations in the effective contact angle and force distribution. Therefore, systematically investigating collision responses by varying impact angles and speeds, and further determining the critical boundary conditions for train derailment, is of great theoretical significance and engineering value for clarifying derailment mechanisms and proposing targeted derailment prevention strategies.

Accordingly, this study establishes a refined train–obstacle collision model using the finite-element (FE) method (Wu et al., 2025; Gür and Cen, 2024). It analyzes the response the train under initial collision angles and impact speeds. Based on the simulation results, a comprehensive analysis is conducted to examine the influence of collision parameters (angle and speed) on dynamics and derailment risk. Finally, a derailment boundary is proposed to critical safety thresholds for speed trains colliding with deformable obstacles

2 Methodology

2.1 Collision model

The high-speed train collision model with obstacle established in this study comprises three interconnected subsystems: the train model, the obstacle model, and the rail model.

This research concentrates on a Chinese high-speed train with a design speed of $250\,\mathrm{km\,h^{-1}}$, developing an FE model for a three-carriage train that includes a head train, middle train, and tail train. According to the requirements of EN 15227 (BSI, 2020), the collision mass is the curb weight under normal operating conditions plus 50 % of the mass of seated passengers, with each passenger weighing 0.08 t. The total collision mass of the train is 167 t.

According to standard EN 15227 (BSI, 2020), honeycomb energy-absorbing devices, train body structure, and bogies were established for the head train. The honeycomb energy-absorbing devices consist of an upper honeycomb energy-absorbing device and a lower device with an anti-creep device. The train body structure includes the pilot frame, underframe, driver's cab, side walls, end walls, and roof. The bogie is mainly composed of a traction seat, a frame, and two wheel sets. The head train model established is depicted in Fig. 1a. The size of the mesh is an important factor affecting the simulation accuracy and computational efficiency of rail trains. In order to balance accuracy and efficiency, in this paper, the head train model was established with a 10 mm grid size for the front part of the train body and a 20 mm grid size for the rear part.

The honeycomb energy-absorbing devices are defined in LS-DYNA (Hallquist, 2007) using MAT26: *MAT_HONEYCOMB and simulated using solid elements. Aluminum 6005A-T6 and 6082-T6 are mainly used for the train body, and stainless steel SUS301L_ST is used for the pilot frame (Zou et al., 2025). These metal materials are defined by MAT24: *MAT_PIECEWISE_LINEAR_PLASTICITY. In the bogie, the connections between the traction seat and the frame, as well as between the frame and the wheel sets, are simulated using 6-degree-of-freedom discrete beam elements. These elements are capable of simulating not only the stiffness of springs, but also the preload of the springs. The frame, traction seat, and wheel sets are defined as *MAT_RIGID, the dampers as SDMAT5, and the lateral stopper between the frame and traction seat as SDMAT8. The bogie suspension parameters are exhibited in Table 1.

To validate the accuracy of the developed FE model, a full-scale impact test of the head train against a rigid wall was performed on a real train test rig. A comparison of the front-end deformation between experimental measurement and numerical simulation is provided in Fig. 2, while the contact force versus compression displacement curves from both test and simulation are illustrated in Fig. 3. The results show a high degree of consistency in both the front-end deformation

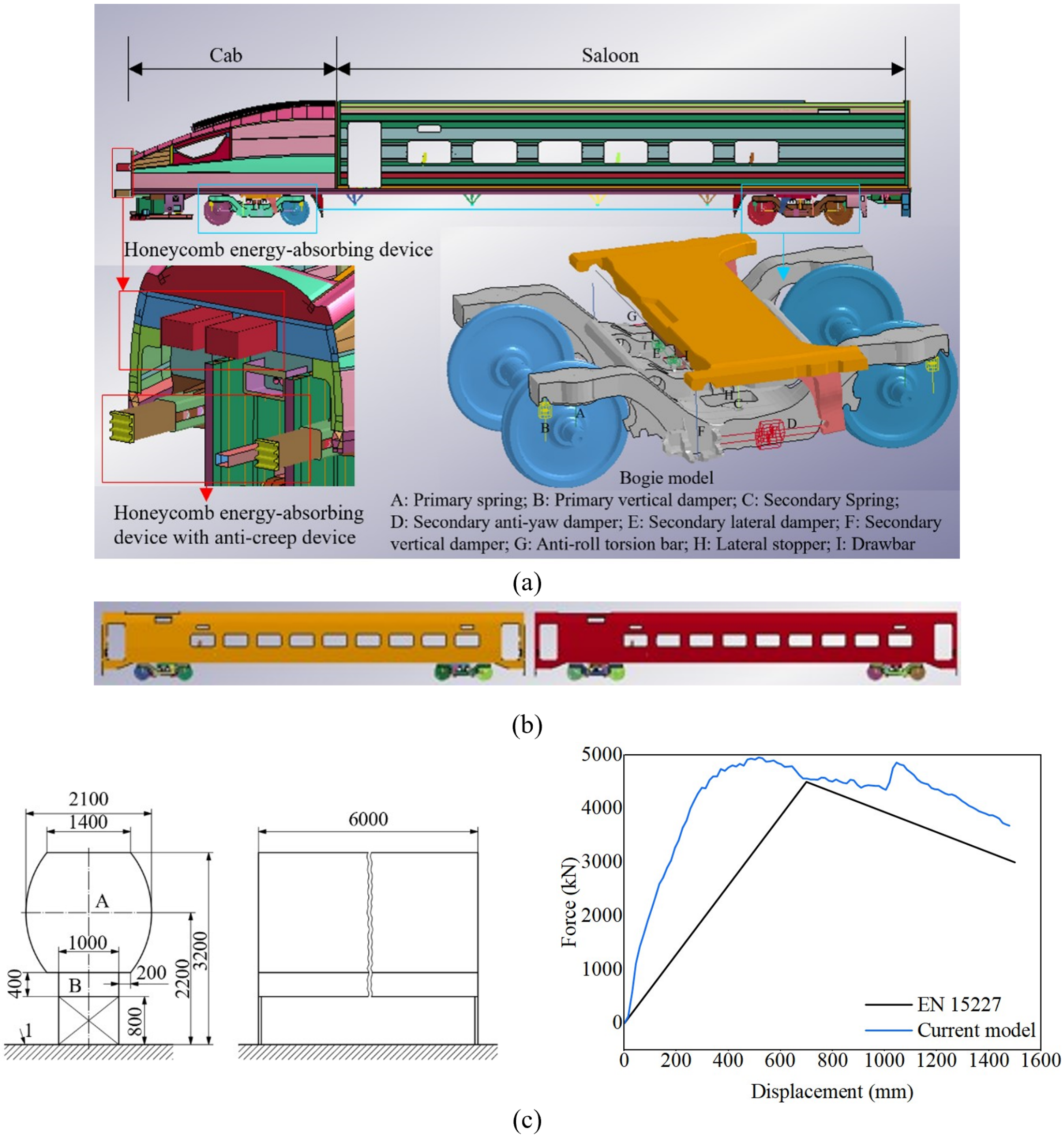

Figure 1. Collision model: **(a)** head train, **(b)** middle train and tail train, and **(c)** obstacle geometry and stiffness (A and B refer to the two parts of the obstacle, and 1 refers to the rail surface).

profile and the force-displacement response, confirming the reliability of the established train FE model.

Based on the modeling method of the head train, the models of a middle and tail train were established, as shown in Fig. 1b. According to standard EN 15227 (BSI, 2020) requirements, the front coupler of the head train should be omitted from the simulation when a train collides with a 15 t deformable obstacle. Therefore, the simulation only includes the middle couplers connecting the head and middle train, as well as those between the middle train and tail train. The middle train coupler is semi-permanent with a gas–liquid buffer on one end and a crush tube on the other. This is simulated using beam elements in LS-DYNA (Hallquist, 2007). A universal joint installed at the coupler base controlled the swing angle of the coupler. The primary design parameters for the middle train coupler are detailed in Table 2.

The geometric shape of the obstacle specified in standard EN 15227 (BSI, 2020) is shown in Fig. 1c. Based on this, an obstacle model was established, and a collision model between the spherical impactor and the obstacle was established to obtain the stiffness of the obstacle. The calculated stiffness is slightly higher than the value specified in EN 15227 (BSI, 2020), which meets the standard requirements (Yao et al., 2024). The rail model is derived from the model of Yao et al. (2020), in which the rail is modeled as a rigid body.

Table 1. Bogie suspension parameters.

Suspension parameters			Numerical value
Primary suspension	Spring	Vertical stiffness ($\mathrm{N\,mm^{-1}}$)	538.1
		Vertical maximum offset (mm)	240
		Longitudinal stiffness ($\mathrm{N\,mm^{-1}}$)	686.3
		Maximum longitudinal offset (mm)	5
		Lateral stiffness ($\mathrm{N\,mm^{-1}}$)	686.3
		Lateral maximum offset (mm)	8
	Damping coefficient of vertical damper ($\mathrm{Ns\,mm^{-1}}$)		10
Secondary suspension	Air spring	Vertical stiffness ($\mathrm{N\,mm^{-1}}$)	173
		Vertical maximum offset (mm)	$+80/-60$
		Longitudinal stiffness ($\mathrm{N\,mm^{-1}}$)	107
		Maximum longitudinal offset (mm)	110
		Lateral stiffness ($\mathrm{N\,mm^{-1}}$)	107
		Lateral maximum offset (mm)	110
	Damping coefficient of anti-hunting shock absorber ($\mathrm{Ns\,mm^{-1}}$)		810
	Damping coefficient of lateral damper ($\mathrm{Ns\,mm^{-1}}$)		15
	Damping coefficient of vertical damper ($\mathrm{Ns\,mm^{-1}}$)		10
Stiffness of anti-roll torsion bar ($\mathrm{N\,mm\,rad^{-1}}$)			4150
Lateral stop stiffness ($\mathrm{N\,mm^{-1}}$)			100
Drawbar stiffness ($\mathrm{N\,mm^{-1}}$)			1250

Table 2. The primary design parameters for the middle train coupler.

Design parameters			Value
Buffer	Stretching	Maximum impedance force (KN)	600
		Maximum stroke (mm)	23
	Compress	Maximum impedance force (KN)	800
		Maximum stroke (mm)	62
Crushable tube		Maximum impedance force (KN)	1500
		Maximum stroke (mm)	380
Coupler swing angle (°)		Horizontal direction	20
		Vertical direction	6

2.2 Boundary condition

In high-speed train collisions with deformable obstacles, automatic single-surface contact is applied to all potential contact scenarios, including self-contacts among components. Furthermore, automatic surface-to-surface contact constraints are defined between wheels and rails, as well as between the train body and the deformable obstacle. The friction coefficient for wheel–rail interaction is set to 0.008 (Li et al., 2019), while that between the train and obstacle is 0.2 (BSI, 2020). The numerical collision model developed for this scenario is illustrated in Fig. 4, where the instantaneous collision angle and speed are denoted as θ and V, respectively, while the initial collision angle and initial speed are defined as θ_0 and v_0.

The instantaneous normal contact force F_n and friction force F_μ at the train–obstacle collision interface are formulated in Eqs. (1) and (2) (Ling et al., 2017).

$$F_\mathrm{n} = \frac{K(K_\mathrm{t}, K_0) \times (X_\mathrm{t} - X_0)}{\cos\theta} \tag{1}$$

$$F_\mu = \mu F_\mathrm{n} \tag{2}$$

Here, $K(K_\mathrm{t}, K_0)$ corresponds to the instantaneous equivalent contact stiffness function between the train and deformable obstacle. X_t and X_0 represent the instantaneous longitudinal deformations of the train and obstacle, respectively, while μ is the contact friction coefficient.

The instantaneous longitudinal and lateral forces acting on the train are formulated in Eqs. (3) and (4) (Ling et al., 2017).

$$F_x = F_\mathrm{n}\cos\theta + F_\mu \sin\theta \tag{3}$$

$$F_z = F_\mathrm{n}\sin\theta F_\mu \cos\theta \tag{4}$$

The train's longitudinal and lateral forces depend directly on θ, highlighting the need to examine its effect on the train–obstacle collision dynamics.

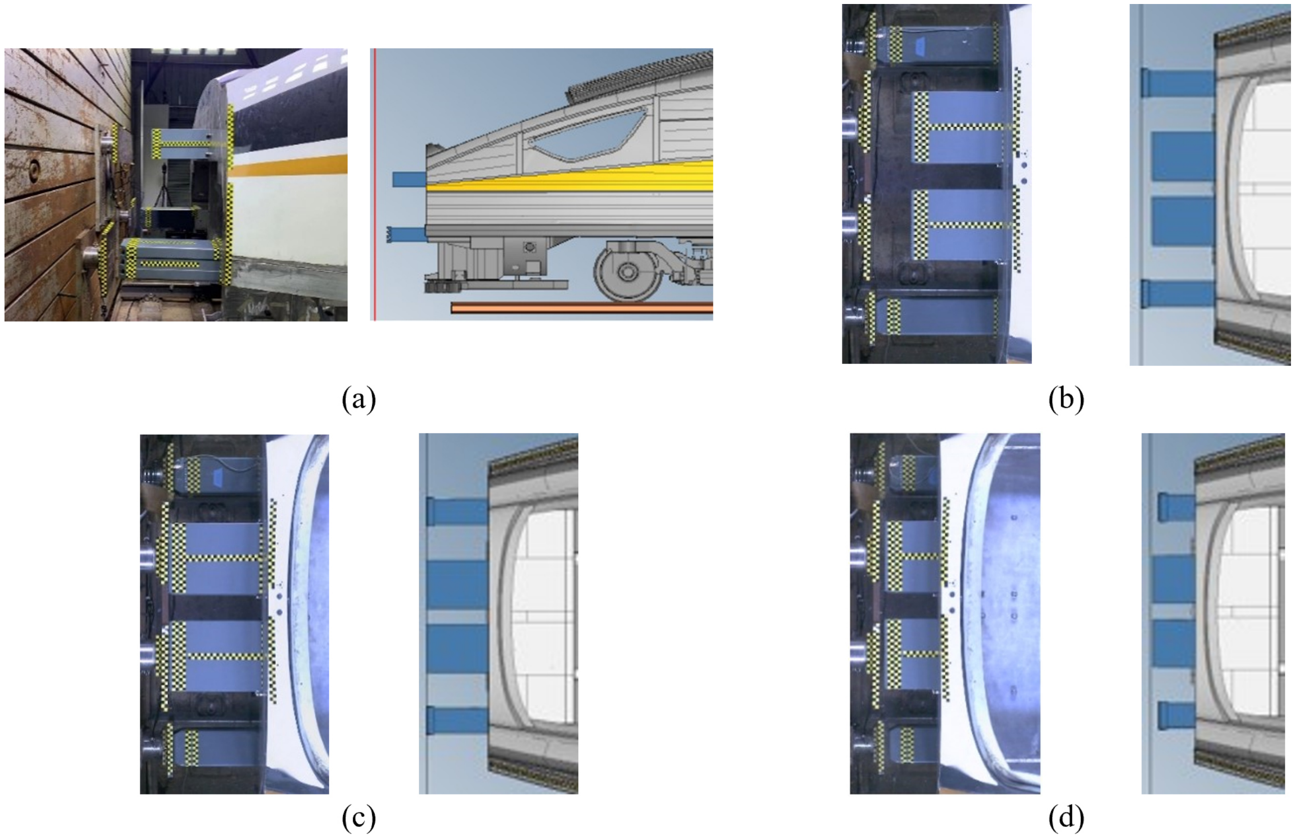

Figure 2. Comparison of the train's front-end crush deformation profiles from the full-scale test and numerical simulation: **(a)** pre-impact initial state, **(b)** impact phase of the lower honeycomb energy-absorbing component against the rigid barrier, **(c)** coordinated compression of both the upper and the lower honeycomb energy-absorbing units, and **(d)** impact rebound state.

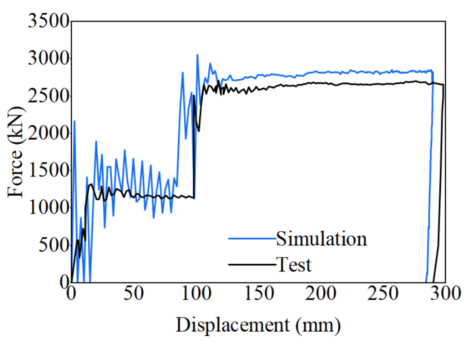

Figure 3. Comparison of contact force–compression displacement curves.

The corresponding energy conservation relation is given in Eq. (5).

$$E_{\mathrm{tv}_0} = E_{\mathrm{tv}_\mathrm{t}} + E_{\mathrm{ov}_\mathrm{t}} + E_{\mathrm{ti}} + E_{\mathrm{oi}} + E_{\mathrm{d}} \tag{5}$$

Each term in the energy conservation principle corresponds to a specific energy component:

- $E_{\mathrm{tv}_0} = \frac{1}{2} m_\mathrm{t} v_0^2$: initial kinetic energy of the train
- $E_{\mathrm{tv}_\mathrm{t}} = \frac{1}{2} m_\mathrm{t} v_\mathrm{te}^2$: kinetic energy of the train after impact
- $E_{\mathrm{ov}_\mathrm{t}} = \frac{1}{2} m_\mathrm{o} v_\mathrm{te}^2$: kinetic energy of the obstacle after impact
- E_{ti}, E_{oi}: internal energies absorbed by the train and obstacle, respectively
- E_d: energy dissipated during the collision due to friction, damping, etc.

Here, m_t and m_o denote the masses of the train and obstacle, v_0 is the train's initial speed, and v_te represents their common speed post-collision.

The momentum conservation equation for this train–obstacle collision is formulated in Eq. (6).

$$m_\mathrm{t} v_\mathrm{o} = m_\mathrm{t} v_\mathrm{te} + m_\mathrm{o} v_\mathrm{te} \tag{6}$$

As documented in prior research, variations in kinetic energy represent a significant factor influencing train derailment (Jun and Qingyuan, 2005). The mathematical expression for this kinetic energy change throughout the collision is given in Eq. (7).

$$E_\mathrm{K} = E_{\mathrm{ti}} + E_{\mathrm{oi}} + E_\mathrm{d} \tag{7}$$

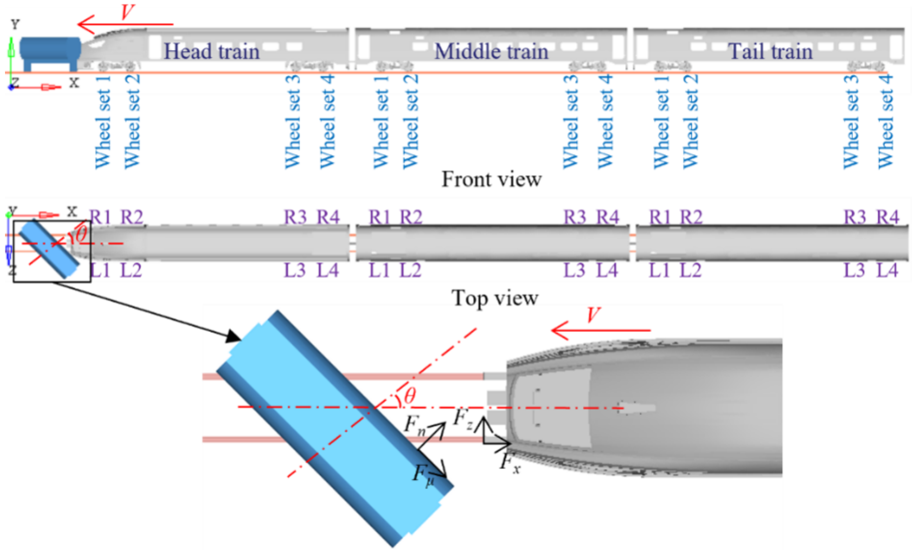

Figure 4. High-speed train-deformable obstacle collision model.

By integrating Eqs. (5) to (7), the expression for kinetic energy change is presented in Eq. (8).

$$E_\mathrm{K} = \frac{m_\mathrm{t} m_\mathrm{o} v_0^2}{2(m_\mathrm{t} + m_\mathrm{o})} \tag{8}$$

For a fixed total mass, the magnitude of kinetic energy variation exhibits a positive correlation with the train's initial collision speed. Thus, increased impact speed not only amplifies energy dissipation but also heightens the risk of derailment.

According to EN 15227 (BSI, 2020), θ_0 is 0° and v_0 is 110 km h^{-1}. In this study, θ_0 spans up to 45°, while v_0 reaches a maximum of 250 km h^{-1}, consistent with the train's design speed. The train's longitudinal (X) direction is defined as the direction of travel. The train's left-to-right direction is defined as the lateral (Z). The train's floor-to-roof direction is defined as the vertical (Y). The wheel set numbers and wheel numbers are illustrated in Fig. 4.

2.3 Evaluation index for train collision derailment

The evaluation criteria for train derailment mainly use the derailment coefficient (DC) and the wheel load reduction rate (WLRR) as the assessment indicators. The safety limit value of DC in this paper is set at 1.2, and the safety limit value of WLRR is set at 0.65 (State Administration for Market Regulation, 2019). The DC ζ was proposed by Nodel and defined as Eq. (9) (Nadal, 1896).

$$\xi = \frac{Q}{P} \tag{9}$$

Here, Q denotes the wheel–rail lateral force, and P represents the vertical force.

WLRR η is defined as Eq. (10).

$$\eta = \frac{\Delta P}{\overline{P}} = \frac{P_\mathrm{L} - P_\mathrm{R}}{P_\mathrm{L} + P_\mathrm{R}} \tag{10}$$

Here, ΔP signifies the wheel load reduction, and $\overline{P}$ corresponds to the mean wheel weight, while P_L and P_R denote the wheel–rail normal forces exerted by the left and right wheels of a single wheel set, respectively.

Furthermore, some scholars use wheel vertical displacement to evaluate train derailment. A train is deemed to have derailed when the wheel vertical displacement exceeds the flange height, meaning the lowest point of the flange is above the rail head (Li et al., 2025; Jin et al., 2012). The wheel–rail model presented in this paper is founded on LMA wheel treads and 60 kg m^{-1} rails (Yao et al., 2020). Therefore, the safety threshold for the vertical displacement of the wheel is 28 mm.

3 Results and discussion

3.1 The influence of the initial collision angle

When the train collided with the obstacle at 110 km h^{-1} and θ_0 ranged from 0 to 45°, the maximum DC for the wheels and WLRR for each wheel set on the head train are listed in Tables 3 and 4, respectively.

When θ_0 was 0°, the DC of all wheels was small. When the initial collision angle was between 5 and 35°, the DC of some wheels of the head train exceeded 1.2. When the initial collision angle was between 40 and 45°, the DC of all wheels of the head train exceeded 1.2. In the instance that θ_0 was 0°, the WLRR of all wheel sets was less than 0.65. With a θ_0 of 5°, the WLRR of wheel set 2 of the head train was slightly less than 0.65, while the remaining wheel sets exceeded 0.65.

Table 3. DC for the wheels. (Note: Bold values indicate DC exceeds 1.2.)

Wheel	Initial collision angle									
number	0°	5°	10°	15°	20°	25°	30°	35°	40°	45°
L1	0.4	**1.3**	**1.9**	**2.0**	**2.1**	**1.9**	**1.4**	**1.8**	**2.3**	**1.7**
R1	0.4	0.4	**1.4**	**1.6**	**2.1**	**2.2**	**2.1**	**2.0**	**2.1**	**2.1**
L2	0.4	0.9	0.5	0.4	0.8	**1.5**	**1.8**	**2.0**	**5.2**	**3.6**
R2	0.4	0.9	**2.1**	**1.9**	**2.1**	**2.1**	**1.9**	**2.2**	**2.0**	**2.1**
L3	0.4	0.5	**1.2**	**1.7**	**2.0**	**1.7**	**1.3**	0.8	1.4	2.1
R3	0.4	0.4	0.4	0.4	0.8	0.8	1.0	**1.9**	**2.1**	**2.0**
L4	0.4	0.4	0.4	0.4	0.7	0.7	**2.6**	**2.3**	**2.3**	**2.7**
R4	0.4	**1.9**	**2.1**	**2.5**	**2.3**	**2.2**	**2.0**	**2.3**	**3.3**	**5.9**

Table 4. WLRR for the wheel sets. (Note: Bold values indicate WLRR exceeds 0.65.)

Wheel set	Initial collision angle									
number	0°	5°	10°	15°	20°	25°	30°	35°	40°	45°
Wheel set 1	0.4	**0.7**	**1.0**	**1.0**	**1.0**	**1.0**	**1.0**	**1.0**	**1.0**	**1.0**
Wheel set 2	0.4	0.6	**0.8**	**1.0**	**1.0**	**1.0**	**0.9**	**1.0**	**1.0**	**1.0**
Wheel set 3	0.4	**0.7**	**0.8**	**0.8**	**0.8**	**0.9**	**0.8**	**1.0**	**1.0**	**1.0**
Wheel set 4	0.3	**0.8**	**1.0**	**1.0**	**1.0**	**1.0**	**1.0**	**1.0**	**1.0**	**1.0**

For initial collision angles between 10 and 45°, the WLRR of all wheel sets on the head train exceeded 0.65. As shown in the above results, as the initial collision angle grew larger, the DC of the wheel and the WLRR of the wheel sets rose, along with the risk of train derailment. However, the simulation results showed that only when the initial collision angle was 45° did the four wheels at the front bogie of the head train derail. From the aforementioned, when the DC and the WLRR exceed the standard, derailment does not necessarily occur. It should also be noted that the DC is the ratio of the wheel–rail lateral force to the vertical force. When the vertical force is zero, the DC cannot be calculated. Therefore, when the wheel is not in contact with the rail, the DC value cannot be obtained. At the same time, the WLRR is the ratio of the difference between the wheel–rail pressure of the left and right wheels of a wheel set to the sum of the pressures. When one side of a wheel set loses contact with the rail, the wheel pressure on that side drops to 0, and the WLRR of that wheel set is 1. However, when both sides of a wheel set lose contact with the rail, the WLRR of that wheel set cannot be obtained. Therefore, the two parameters of WLRR and DC cannot accurately evaluate the wheel derailment phenomenon.

Among all the derailment scenarios investigated, only the wheels on the front bogie of the head train experienced derailment. Accordingly, the analysis concentrated on the dynamic behavior of the head vehicle. As illustrated in Fig. 5, the displacements of the wheel L1 of the head train under different collision angles are demonstrated. The vertical displacement tended to increase as θ_0 increased. When θ_0 was 0 to 30°, the vertical displacement was small. When θ_0 was 35°, the vertical displacement was 11.9 mm. When θ_0 increased to 40°, the vertical displacement was 24.9 mm. That is, when θ_0 was less than 40°, the vertical displacement did not exceed 28 mm. When θ_0 increased to 45°, wheel L1 lifted 42.8 mm. Similarly, the lateral displacement of wheel L1 also tended to increase as θ_0 increased. When θ_0 was between 0 and 40°, the lateral displacement was relatively small. When θ_0 was 45°, the lateral displacement increased to 427.2 mm.

When θ_0 reached 45°, the wheel exhibited a substantial increase in vertical and lateral displacements, requiring further analysis of this scenario. The displacement variations in L1 (left wheel) and R1 (right wheel) in wheel set 1 are illustrated in Fig. 6a. As shown in Fig. 6b and c, the wheel–rail contact forces, which exhibit variability and nonlinearity, cannot be directly measured during train operation (Zhao et al., 2023; Guo et al., 2025) but can be obtained through simulation. The figure shows the wheel set from the rear, with L1 on the left and R1 on the right.

Approximately 0.03 s after the collision, the left wheel, L1, began to lift. At this point, the wheel–rail force of wheel L1 became zero. Meanwhile, the vertical and lateral forces of wheel R1 on the rail increased. This caused the wheel to roll over to the right. Wheel L1 raised to a height of 42.8 mm at approximately 0.07 s. It then landed on the rail at around 0.14 s. From this point onward, the vertical and lateral wheel–rail forces initiated an upward trend starting at zero. Wheel L1 climbed the rail, moving laterally to the left, with the flange gradually ascending onto the rail. It continued moving to the left. As the lateral displacement of the wheel

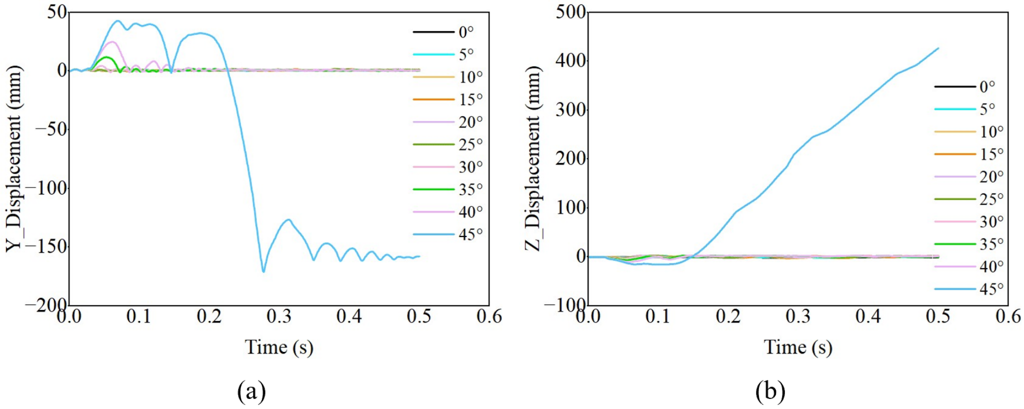

Figure 5. Displacement of head train wheel L1: **(a)** vertical displacement and **(b)** lateral displacement.

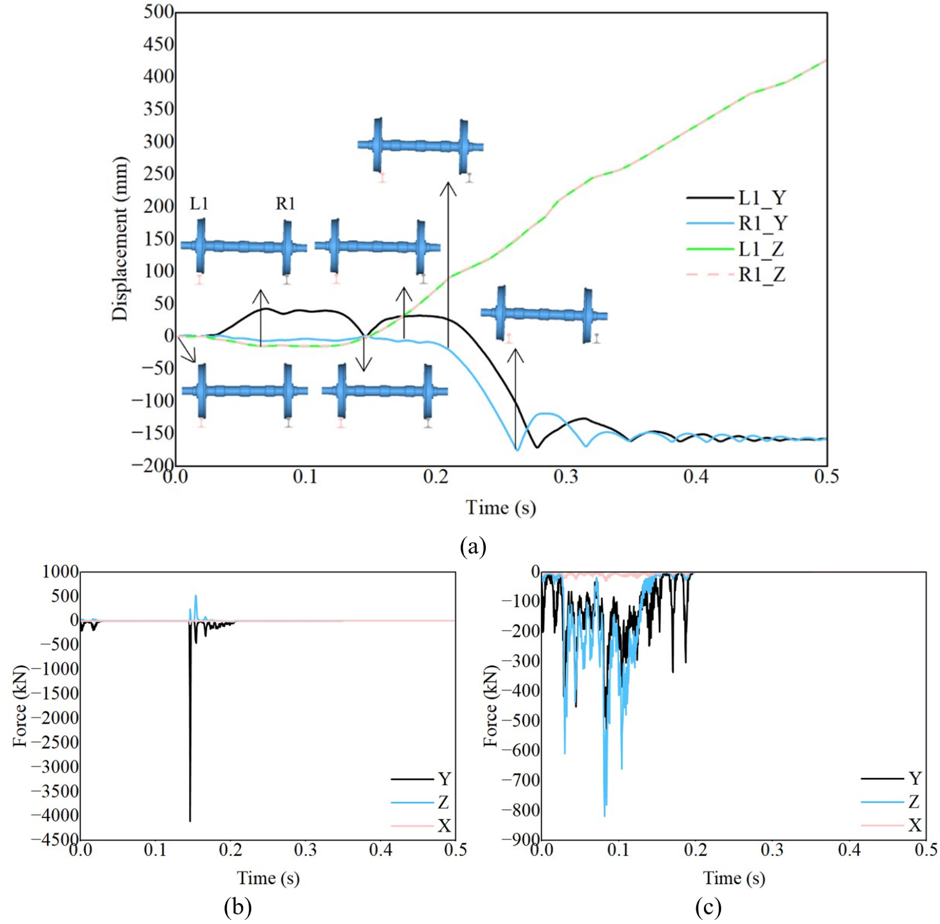

Figure 6. Dynamic state of wheels L1 and R1 in the full duration of the collision: **(a)** displacement of wheels L1 and R1, **(b)** wheel–rail force of wheel L1, and **(c)** wheel–rail force of wheel R1.

continued to increase, the contact force between wheel L1 and the rail became zero at approximately 0.21 s, causing the wheel to derail. This was a climbing derailment. Wheel R1 did not lift during the collision but slid to the left. At around 0.20 s, the wheel–rail contact force dropped to zero, and the wheel was no longer constrained by the rail, resulting in derailment.

It is worth noting that the left wheel, L1, first experienced a lift of more than 28 mm but did not derail. It then landed on the rail and rose again. When the vertical displacement exceeded 28 mm again, derailment occurred. The vertical displacement of the right wheel, R1, remained below 28 mm, indicating that wheel vertical displacement partially reflects derailment risk, but its predictive capability has limitations.

When the lowest position of the wheel flange surpasses the rail surface, the wheel loses constraint from the rail; however, actual derailment only occurs after sufficient lateral displacement takes place. For this reason, the lateral displacement is further analyzed in this study. The wheel–rail interaction model established in this paper adopts the LMA wheel tread profile and a 60 kg m^{-1} rail (Yao et al., 2020). The safe value for the lateral displacement of the wheel should be 55 mm (Zou et al., 2025). When the lateral displacement of wheel L1 exceeded 55 mm, the wheel derailed, as shown in Fig. 6a. The prerequisite for this phenomenon was that the vertical displacement surpassed the flange height of 28 mm and the flange constraint, allowing continued lateral movement. In other words, if the wheel vertical displacement of one wheel exceeds 28 mm and the lateral displacement exceeds 55 mm, then the wheel set will derail. Therefore, wheel vertical displacement and lateral displacement can be combined to evaluate wheel derailment.

3.2 The influence of the initial collision speed

The front-end deformation is shown in Fig. 7, with θ_0 at 0° and v_0 set to a range of 110 to 250 km h^{-1}. At a collision speed of 110 km h^{-1}, the upper honeycomb energy-absorbing device at the front end of the head train was almost completely compressed. Meanwhile, the lower honeycomb energy absorber integrated with an anti-creep device was compressed to a small extent. Additionally, the front end of the train was slightly dented when it hit the obstacle. When v_0 increased to 140 km h^{-1}, the deformation of the train body became more severe. At 170 km h^{-1}, the driver's cab became severely deformed. At 200 km h^{-1}, it was compressed to half its original size. At 250 km h^{-1}, the entire driver's cab became deformed, as did the front door area of the saloon. With rising v_0, the deformation of the train was aggravated, a phenomenon associated with the longitudinal force acting on the contact interface, as shown in Fig. 8a. With a higher collision speed, the kinetic energy of the train increased, and the longitudinal contact force also increased so that the train undergoes more deformation to absorb the increased kinetic energy.

As illustrated in Fig. 9a, the vertical displacements of wheel L1 of the head train under different collision speeds are demonstrated. When v_0 was between 110 and 140 km h^{-1}, vertical displacements of wheel L1 did not exceed 28 mm. For v_0 in the 170–250 km h^{-1} interval, wheel L1 exhibited a sustained separation from the rail, with a vertical displacement exceeding 28 mm. The vertical displacement increased monotonically with the increase in speed. The generation of the vertical displacement was related to the vertical force of the contact interface, as shown in Fig. 8b. As the collision speed increased, the vertical contact interface force increased, causing the vertical displacement to increase.

The lateral displacements of leading wheel L1 under different collision speeds are shown in Fig. 9b. When v_0 was between 110 and 140 km h^{-1}, the wheels moved laterally toward a certain distance before the wheel flange collided with the rail. Then, the wheels moved in the opposite direction, resulting in a positive and negative oscillation phenomenon in lateral displacement with a small amplitude. The lateral displacement of the wheels increased with the increase of v_0 from 170 to 250 km h^{-1}, though it never exceeded 55 mm. The generation of the lateral displacement was related to the lateral force of the contact interface, as shown in Fig. 8c. As v_0 increased, the lateral contact interface force increased, causing the lateral displacement to increase.

When v_0 reached the designed speed of 250 km h^{-1}, wheel L1 significantly deviated from the rail and stayed separated for a long time. The wheels of wheel set 1 of the head train are taken as an example to discuss the dynamic state in the full duration of the collision. The displacement curves of wheels L1 and R1 are shown in Fig. 10a, which shows the status of wheel set 1 at different times. The wheel–rail forces of wheels L1 and R1 are shown in Fig. 10b and c.

At about 0.16 s, the left wheel, L1, underwent its first upward displacement, causing the wheel–rail contact force to reduce to zero. The right wheel, R1, followed closely behind and lifted off the rail at approximately 0.18 s, with the contact force also dropping to zero. Wheel R1 reached its maximum height of 358.2 mm at about 0.31 s, and wheel L1 reached its maximum height of 346.7 mm at about 0.33 s. Then, the wheels began to descend. As they disengaged from the rail constraints, the wheels underwent slight lateral displacement. At 0.57 s, the lateral displacement of the wheel L1 and R1 moving to the right reached its maximum value of 27.5 mm. The wheel flange of wheel R1 landed on the rail at approximately 0.63 s, with the contact force increasing from zero. The flange ran along the rail surface and gradually slid to the left. Around 0.71 s, the flange slid down along the rail, leading to the recovery of normal wheel–rail contact. At this moment, the vertical component of the wheel–rail contact force reached a maximum of 4,042.7 kN. After this, the wheel ran normally along the rail surface. At approximately 0.65 s, the left wheel, L1, re-established contact with the rail surface. The contact force then rose from zero, after which rebound occurred and the contact force dropped back to zero. The wheel then descended again, and at 0.67 s, the contact force increased from zero and the wheel operated normally. The wheel did not derail during the entire collision. This once again proved that vertical displacement alone cannot be used to evaluate wheel derailment.

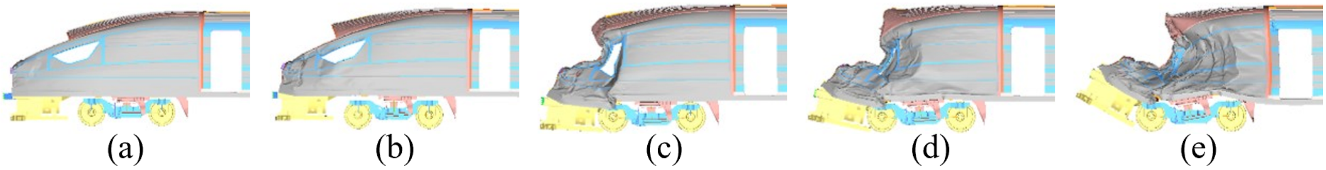

Figure 7. Front end deformation diagram at different collision speeds: **(a)** $110\,\mathrm{km\,h^{-1}}$, **(b)** $140\,\mathrm{km\,h^{-1}}$, **(c)** $170\,\mathrm{km\,h^{-1}}$, **(d)** $200\,\mathrm{km\,h^{-1}}$, and **(e)** $250\,\mathrm{km\,h^{-1}}$.

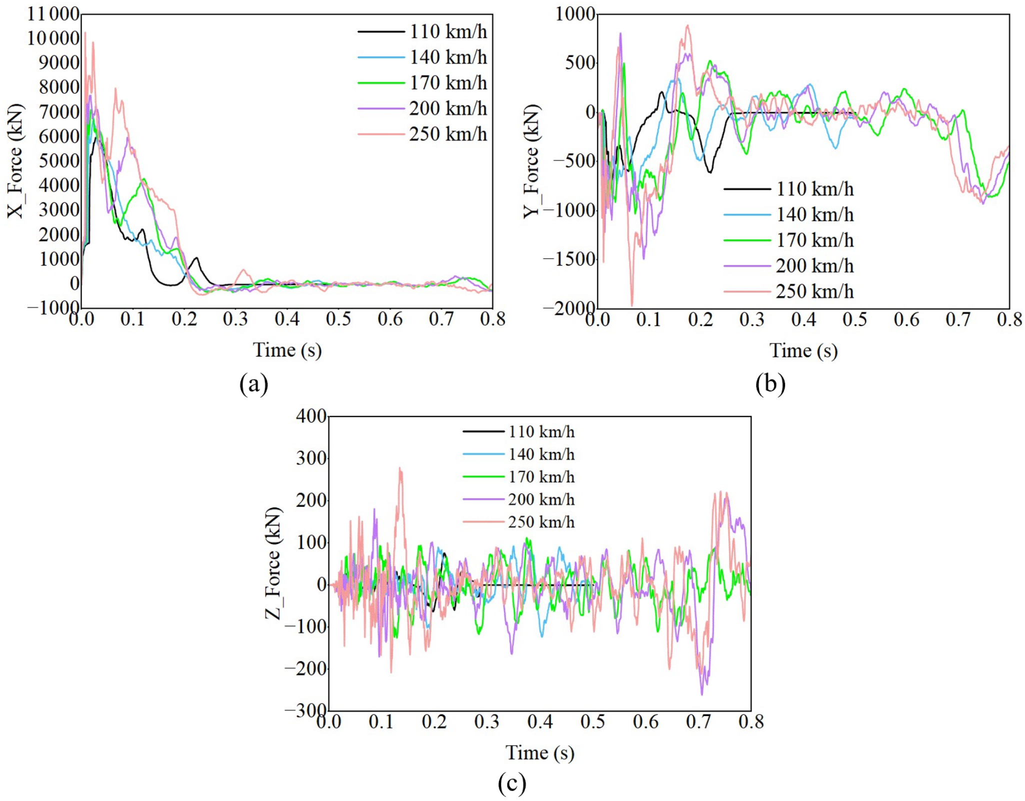

Figure 8. Collision interface contact force: **(a)** longitudinal force, **(b)** vertical force, and **(c)** lateral force.

3.3 Train derailment boundary

The initial collision angle θ_0 was set from 0 to 45° with an interval of 5°. The initial collision speed v_0 was determined based on the speed $110\,\mathrm{km\,h^{-1}}$ specified in EN 15227. For each angle, if no derailment occurred at $110\,\mathrm{km\,h^{-1}}$, the speed was increased stepwise by $10\,\mathrm{km\,h^{-1}}$ up to the design speed of $250\,\mathrm{km\,h^{-1}}$. If derailment was observed at $110\,\mathrm{km\,h^{-1}}$, the speed was decreased stepwise by $10\,\mathrm{km\,h^{-1}}$ to locate the critical condition. The critical speed at each angle was determined accordingly, and linear interpolation was adopted to obtain intermediate values. The derailment boundary was then established by connecting these critical speeds at each collision angle, as presented in Fig. 11.

Notably, when the initial collision angle was between 0 and 5°, the train would not derail even when v_0 increased to the train's design speed of $250\,\mathrm{km\,h^{-1}}$. This demonstrates that, with a small initial collision angle, the train is less likely to derail. When θ_0 increased, derailment initiation speed generally decreased. When θ_0 increased to 10, 15, 20, and 25°, the train derailed at speeds of 200, 190, 180, and $150\,\mathrm{km\,h^{-1}}$, respectively. As the initial collision angle increased to 30, 35, 40, and 45°, the corresponding speeds reached 140, 150, 150, and $50\,\mathrm{km\,h^{-1}}$, at which point the train derailed.

Depending on the process of train derailment, various types of derailment can occur, such as jumping derailment and climbing derailment. An analysis of different train derailment modes showed that jumping derailment occurred in scenarios on the derailment boundary when the initial collision angle was between 10 and 25°. In these scenarios, after the collision occurred, the wheels on the front bogie of the head train rose significantly, then fell, accompanied by a large amount of lateral displacement. During the fall, the wheels might have brief contact or no contact with the rail, but they

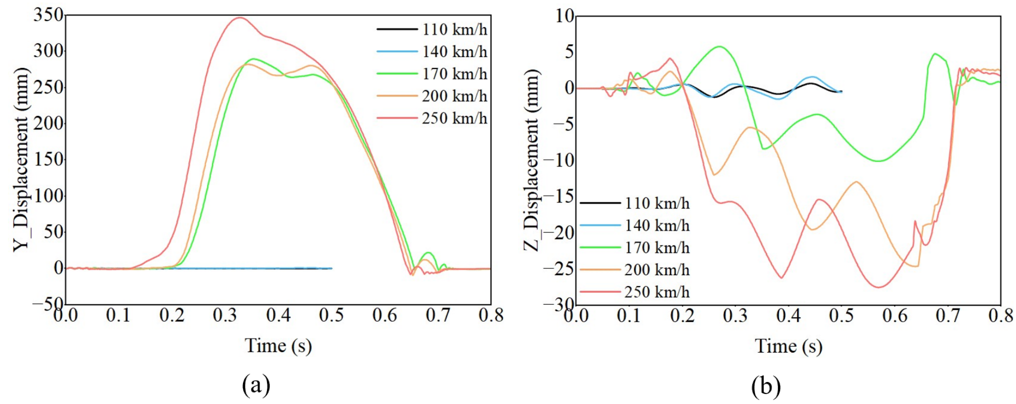

Figure 9. Displacement of head train wheel L1: **(a)** vertical displacement and **(b)** lateral displacement.

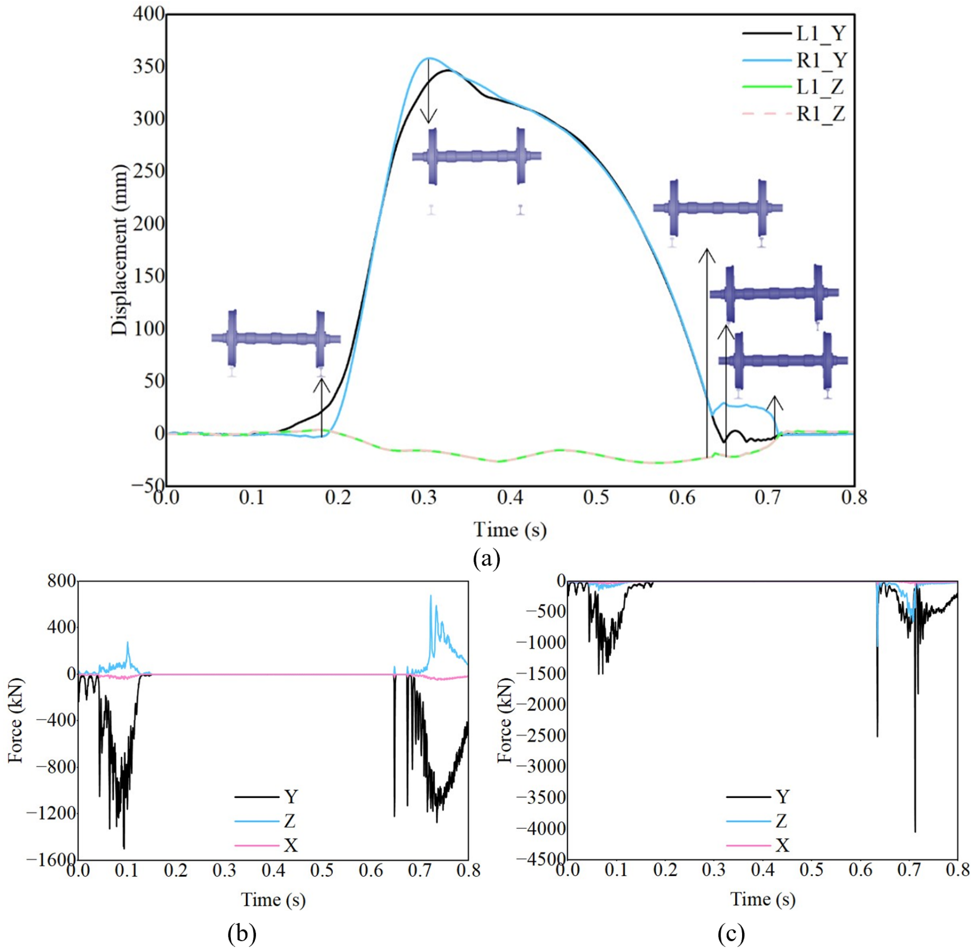

Figure 10. Dynamic state of wheels L1 and R1 in the full duration of the collision: **(a)** displacement of wheels L1 and R1, **(b)** wheel–rail force of wheel L1, and **(c)** wheel–rail force of wheel R1.

would not return to their normal operating state. Eventually, the wheels lost the constraint of the rail and derailed. When the initial collision angle was between 30 and 45°, some of the wheels on the front bogie of the head train in each scenario on the derailment boundary underwent climbing derailment. Climbing derailment refers to the flange climbing onto the rail, running on the rail surface, and generating lateral displacement toward the outside of the rail, thereby causing the wheel to derail.

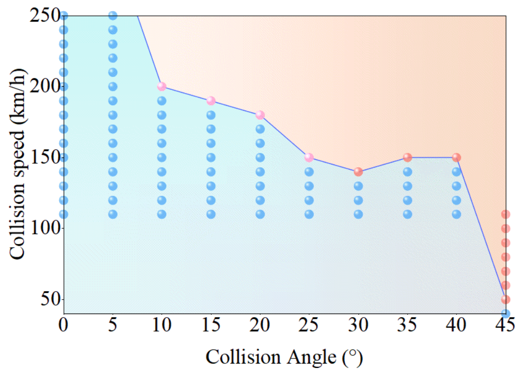

Figure 11. Train derailment boundary.

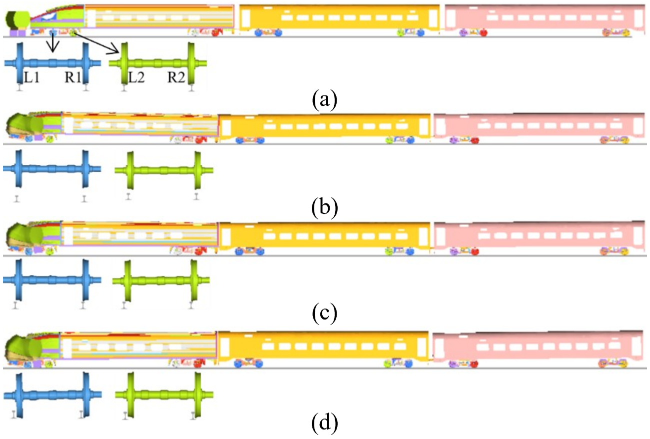

Figure 12. State of the train in the full duration of the collision: **(a)** 0.0 s, **(b)** 0.34 s, **(c)** 0.55 s, and **(d)** 0.66 s.

In the scenarios on the derailment boundary where the initial collision angle was between 10 and 25°, the wheels underwent jumping derailment. Taking the initial collision angle of 10° and the speed of 200 km h^{-1} as an example, the state of the train during the entire collision process was analyzed, as shown in Fig. 12. The initial state of the train is shown in Fig. 12a, with each wheel in proper contact with the rail. After the collision, the wheels of the front bogie of the head train began to lift. At 0.34 s, the wheels of wheel set 1 reached its highest position, as shown in Fig. 12b. Then the wheels descended. At about 0.55 s, wheel R1 came into contact with the top surface of the rail, as shown in Fig. 12c. Due to the excessive lateral displacement of the wheels, the wheels failed to regain normal contact with the rail and continued to descend. At 0.66 s, the wheels dropped to the ground, as shown in Fig. 12d. The movement states of the wheels on the same side of the same bogie were basically the same, such as L1, L2, R1, and R2.

On the derailment boundary, when θ_0 was between 30 and 45°, the wheels on the front bogie of the head train underwent climbing derailment. Taking an initial collision angle of 30° and a speed of 140 km h^{-1} as an example, the state of the train during the entire collision process is shown in Fig. 13. The initial configuration is presented in Fig. 13a. At 0.05 s, the left wheel, L1, of wheel set 1 exhibited a slight lift, as depicted in Fig. 13b, and then dropped onto the rail and resumed normal contact with the rail at 0.08 s, as shown in Fig. 13c. After a brief normal operation, wheel L1 began to climb the rail, with the flange rising to the top of the rail at 0.30 s, as shown in Fig. 13d. It then continued to drift laterally at 0.39 s, resulting in derailment, as shown in Fig. 13e, and landed on the ground at 0.46 s, as shown in Fig. 13f. The right wheel, R1, did not lift at all. As the wheel set continued to drift laterally, the tread of the right wheel, R1, slid along the top of the rail until it derailed.

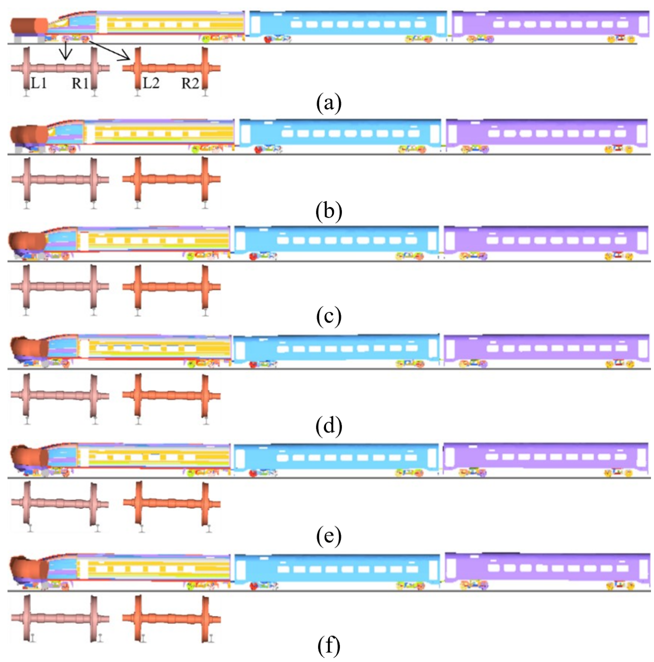

Figure 13. State of the train in the full duration of the collision: **(a)** 0.0 s, **(b)** 0.05 s, **(c)** 0.08 s, **(d)** 0.30 s, **(e)** 0.39 s, and **(f)** 0.46 s.

This coupled angle–speed derailment boundary serves as the critical safety threshold for high-speed trains colliding with deformable obstacles, enabling quantitative safety assessment and supporting the classification of distinct derailment mechanisms under varying impact conditions.

4 Conclusions

This study systematically analyzed the dynamic responses of high-speed trains during collisions with deformable obstacles at various initial collision angles θ_0 and speeds v_0 and further established a derailment boundary model considering the angle–speed coupling effect.

1. With v_0 fixed at 110 km h^{-1}, the DC, WLRR, and vertical and lateral displacement of the wheels all showed an upward trend as θ_0 increased from 0 to 45°. At the

45° collision angle, derailment occurred, which could be evaluated by analyzing the combined vertical and lateral wheel displacements.

2. At the 0° collision angle, even as v_0 increased from 110 to 250 $\mathrm{km\,h^{-1}}$, the wheel's displacement increased with speed, but no derailment occurred. Vertical displacement was associated with the vertical contact force, lateral displacement with the lateral contact force, and train body deformation with the longitudinal contact force generated during the train–obstacle collision. Derailment was induced by the combined effects of lateral and vertical forces at the contact interface.

3. Two distinct derailment modes (jumping and climbing) are identified and linked to collision angle, providing a clear physical mechanism for derailment prevention. When θ_0 was less than 5°, derailment did not take place even at the design speed of 250 $\mathrm{km\,h^{-1}}$. By contrast, when θ_0 increased to the range of 10–25°, jumping derailment occurred at speeds between 150 and 200 $\mathrm{km\,h^{-1}}$. As θ_0 continued to rise to 30–45°, climbing derailment was observed within the speed interval of 50 to 150 $\mathrm{km\,h^{-1}}$.

These findings provide practical safety guidelines for railway infrastructure design and operational speed limits. The derailment boundary analysis shows that smaller initial collision angles are associated with lower derailment risk, which may provide a useful reference for the design and layout of railway intersections. Larger angles lower derailment speed thresholds, suggesting speed limits at high-risk areas like level crossings. Future research could focus on quantifying safety margins for high-speed railways under natural disasters, particularly through multi-hazard coupling analysis (e.g., mudslides, earthquakes, extreme weather events).

Data availability. The data supporting the findings of this study are available from the corresponding author upon reasonable request. The finite-element model setup, simulation parameters, and post-processing results are not publicly available due to ongoing related research projects but can be provided for verification purposes with permission.

Author contributions. Lingxiang Kong: writing – original draft, software, data curation. Shuguang Yao: writing – review and editing. Dongtao Wang: supervision, methodology, conceptualization.

Competing interests. The contact author has declared that none of the authors has any competing interests.

Disclaimer. Publisher's note: Copernicus Publications remains neutral with regard to jurisdictional claims made in the text, published maps, institutional affiliations, or any other geographical representation in this paper. The authors bear the ultimate responsibility for providing appropriate place names. Views expressed in the text are those of the authors and do not necessarily reflect the views of the publisher.

Acknowledgements. This work was supported by the Hunan Provincial Department of Education Scientific Research Outstanding Youth Project (no. 25B1060) and the Hunan Provincial Natural Science Foundation (no. 2023JJ60216).

Financial support. This research has been supported by the Hunan Provincial Department of Education Scientific Research Outstanding Youth Project (grant no. 25B1060) and the Natural Science Foundation of Hunan Province (grant no. 2023JJ60216).

Review statement. This paper was edited by Liangliang Cheng and reviewed by two anonymous referees.

References

BSI: EN 15227: Railway applications – Crashworthiness requirements for rail vehicles, https://doi.org/10.31030/2846185, 2020.

Cho, H. J. and Koo, J. S.: A numerical study of the derailment caused by collision of a rail vehicle using a virtual testing model, Vehicle Syst. Dyn., 50, 79–108, https://doi.org/10.1080/00423114.2011.563860, 2012.

Guo, X., He, H., and Cao, D.: Estimation of wheel-rail contact force based on extended kalman filter, Int. J. Dynam. Control., 13, 1–21, https://doi.org/10.1007/s40435-025-01775-7, 2025.

Gür, Y. and Cen, G.: Comparison of finite element analysis results with strain gauge measurements of a front axle housing, Mech. Sci., 15, 257–268, https://doi.org/10.5194/ms-15-257-2024, 2024.

Hallquist, J. O.: LS-DYNA keyword user manual (version 971), Livermore Software Technology Corporation, https://ftp.lstc.com/anonymous/outgoing/jday/manuals/ (last access: 22 April 2026), 2007.

Hou, L., Peng, Y., and Sun, D.: Dynamic analysis of railway vehicle derailment mechanism in train-to-train collision accidents, P. I. Mech. Eng. F-J. Rail., 235, 1022–1034, https://doi.org/10.1177/0954409720959870, 2020.

Jiang, T. and Chen, J. X.: Facts report on the Taroko Express train accident released, People's Daily Online, http://tw.people.com.cn/n1/2021/0824/c14657-32204848.html (last access: 22 April 2026), 2021.

Jin, X. S., Xiao, X. B., and Ling, L.: Study on the safety boundary for high speed trains in severe environments, Proceedings of the 1st International Workshop on High-Speed and Intercity Railways, 147, 201–224, https://doi.org/10.1007/978-3-642-27960-7_19, 2012.

Jun, X. and Qingyuan, Z.: A study on mechanical mechanism of train derailment and preventive measures for derailment, Vehicle Syst. Dyn., 43, 121–147, https://doi.org/10.1080/00423110412331322201, 2005.

Li, B., Lu, Z., Yan, K., Lu, S., Kong, L., and Xu, P.: Experimental study of a honeycomb energy-absorbing device for high-speed trains, P. I. Mech. Eng. F-J. Rail., 234, 1170–1183, https://doi.org/10.1177/0954409719882564, 2019.

Li, H., Wang, Y., Zeng, J., Li, F., Yang, Z., Mei, G., Gao, H., and Ye, Y.: Fusing binocular vision and deep learning to detect dynamic wheel-rail displacement of high-speed trains, Mech. Syst. Signal Pr., 223, 1–18, https://doi.org/10.1016/j.ymssp.2024.111832, 2025.

Li, Z., Zhu, T., Xiao, S. Zhang, J., Wang, X., and Ding, H.,: Simulation method for train curve derailment collision and the effect of curve radius on collision response, Proc. Inst. Mech. Eng. F-J. Rail., 237, 1130–1139, https://doi.org/10.1177/09544097231154313, 2023.

Ling, L., Dhanasekar, M., Thambiratnam, D. P., and Sun, Y.: Lateral impact derailment mechanisms, simulation and analysis, Int. J. Impact. Eng., 94, 36–49, https://doi.org/10.1016/j.ijimpeng.2016.04.001, 2016a.

Ling, L., Guan, Q., Dhanasekar, M., and Thambiratnam, D. P.: Dynamic simulation of train–truck collision at level crossings, Vehicle Syst. Dyn., 55, 1–22, https://doi.org/10.1080/00423114.2016.1240811, 2016b.

Ling, L., Dhanasekar, M., and Thambiratnam, D. P.: Frontal collision of trains onto obliquely stuck road trucks at level crossings: Derailment mechanisms and simulation, Int. J. Impact. Eng., 100, 154–165, https://doi.org/10.1016/j.ijimpeng.2016.11.002, 2017.

Ling, L., Dhanasekar, M., Wang, K., Zhai, W., and Weston, B.: Collision derailments on bridges containing ballastless slab tracks, Eng. Fail. Anal., 105, 869–882, https://doi.org/10.1016/j.engfailanal.2019.07.042, 2019.

Liu, X., Saat, M. R., and Barkan, C. P.: Analysis of causes of major train derailment and their effect on accident rates, Transport. Res. Rec., 2289, 154–163, https://doi.org/10.3141/2289-20, 2012.

Liu, X., Saat, M. R., and Barkan, C. P.: Freight-train derailment rates for railroad safety and risk analysis, Accident Anal. Pre., 98, 1–9, https://doi.org/10.1016/j.aap.2016.09.012, 2017.

Lu, S., Wang, P., Ni, W., Yan, K. B., Zhao, S., Yang, C. X., and Xu, P.: Energy absorption design for crash energy management passenger trains based on scaled model, Struct. Multidiscip. O., 65, 1–17, https://doi.org/10.1007/s00158-021-03116-6, 2021.

Madsen, P. M., Dillon, R. L., Triantis, K. P., and Bradley, J. A.: The relationship between freight train length and the risk of derailment, Risk. Anal., 44, 2616–2628, https://doi.org/10.1111/risa.14321, 2024.

Nadal, M. J.: Theorie de la stabilite des locomotives. Part II: mouvement de lacet, Ann. Mines, 10, 232, 1896.

Neves, R. R., Fransplass, H., Langseth, M., Driemeier, L., and Alves, M.: Performance of some basic types of road barriers subjected to the collision of a light vehicle, J. Braz. Soc. Mech. Sci. Eng., 40, 1–14, https://doi.org/10.1007/s40430-018-1201-x, 2018.

Peng, Y., Deng, M., Yu, Y. Y., Hu, Z. S., Wang, K., Wang, X., Yi, S. E., and Deng, G. X.: Analysis of moose motion trajectory after bullet train-moose collisions, Eng. Fail. Anal., 151, 1–23, https://doi.org/10.1016/j.engfailanal.2023.107373, 2023.

State Administration for Market Regulation: GB/T 5599-2019, Specification for dynamic performance assessment and testing verification of rolling stock, 2019.

Wu, Z., Pan, W., Niu, R., and Liu, L.: Frame design and improvement of a small electric vehicle, Mech. Sci., 16, 263–272, https://doi.org/10.5194/ms-16-263-2025, 2025.

Yan, Q., Sun, M., Qing, S., Deng, Z., and Dong, W.: Numerical investigation on the damage and cracking characteristics of the shield tunnel caused by derailed high-speed train, Eng. Fail. Anal., 108, 1–15, https://doi.org/10.1016/j.engfailanal.2019.104205, 2020.

Yao, S., Zhu, H., Yan, K., Liu, M., and Xu, P.: The derailment behaviour and mechanism of a subway train under frontal oblique collisions, Int. J. Crashworthines., 26, 133–146, https://doi.org/10.1080/13588265.2019.1692506, 2019.

Yao, S., Zhu, H., Liu, M., Li, Z., Xu, P., and Che, Q.: A study on the frontal oblique collision-induced derailment mechanism in subway vehicles, P. I. Mech. Eng. F-J. Rail., 234, 584–595, https://doi.org/10.1177/0954409719852478, 2020.

Yao, S., Kong, L., Xu, P., Xiao, X., and Peng, Y.: Investigation on the dynamic characteristic of occupant during the frontal collision between high-speed train and obstacle, Accident. Anal. Prev., 199, 1–13, https://doi.org/10.1016/j.aap.2024.107495, 2024.

Yuan, W., Zhu, T., Ding, H., Wang, X., Zhang, J., Lv, T., and Xiao, S.: A study of the collision derailment behaviour of trains based on rail vehicle collision dynamics, P. I. Mech. Eng. F-J. Rail., 240, 84–97, https://doi.org/10.1177/09544097251379280, 2026.

Zhang, T., Guo, X., Jin, T., Yang, Y., Ling, L., Wang, K., and Zhai, W.: Dynamic derailment behaviour of urban tram subjected to lateral collision, Int. J. Rail Transp., 10, 581–605, https://doi.org/10.1080/23248378.2021.1964392, 2021.

Zhang, W. and Li, C.: Numerical simulation of heavy rail transit vehicle collision and analysis of collision force characteristics, J. Vibroeng., 25, 567–580, https://doi.org/10.21595/jve.2022.22942, 2023.

Zhao, A., Huang, J., and Sun, J.: Estimation of wheel–rail structural interactions from motion signals of high-speed train bogie, Int. J. Dynam. Control., 11, 1609–1620, https://doi.org/10.1007/s40435-022-01085-2, 2023.

Zhou, H., Wang, W., and Hecht, M.: Three-dimensional derailment analysis of a crashed city tram, Vehicle Syst. Dyn., 51, 1200–1215, https://doi.org/10.1080/00423114.2013.790553, 2013.

Zhuo, T., Guan, W., Yu, Y., and Gao, G.: Derailment of freight train under frontal oblique collision: Analysis, prevention and test, Mech. Based. Des. Struc., 52, 5637–5652, https://doi.org/10.1080/15397734.2023.2260458, 2023.

Zou, F., Yao, S., Xu, P., Xing, J., Xie, M., and Yang, L.: Frontal collision of trains onto offset obstacles at level crossings: Derailment mechanisms and simulation, Alex. Eng. J., 133, 182–206, https://doi.org/10.1016/j.aej.2025.11.014, 2025.